6th International Conference

on

Wind Turbine Noise

Glasgow 20-23 April 2015

On the Measurement and Prediction of Wind-Turbine Swishing Noise

Cheolung Cheong[†], Oksana Stalnov*, Phillip Joseph*

[†] *Pusan National University, Pusan 609-735, Republic of Korea*

**University of Southampton, England SO17 1BJ, United Kingdom*

1. Introduction

Wind turbine noise is one of the main factors that limit the widespread exploitation of wind energy. The periodic 'swishing' character of wind turbine noise is often reported as an important factor in explaining its relatively high annoyance compared to other sound sources of roughly the same level [1, 2]. Swishing is the result of an amplitude modulation of the broadband aerodynamic noise, which occurs at the blade passing frequency, and is typically about 1 Hz for modern large horizontal-axis wind turbines. This paper has three objectives: The first is to present a new tool for the analysis of wind turbine noise data and swishing noise in particular. It is based on cyclostationary analysis, which is ideally suited to the analysis of data whose statistics vary periodically in time. The second is to present a prediction method based on Amiet's model of rotor noise. It is based on the concept of instantaneous spectrum from which the time variation of the noise spectrum may be deduced. Noise predictions from this model will be compared against the cyclostationary measurements from a modern wind turbine. The third is to develop an index to assess the swishing noise of wind turbine. A relative simple algebraic formulation is proposed to formulate this index, which is of use in the understanding of wind turbine swishing character.

Several studies [3-8] have been performed aimed at characterizing the amplitude modulation of wind turbine noise and the understanding of its mechanisms. Most of these studies [3-7] are experimental but include predictions and interpretation based on simple theoretical considerations. Dunbabin [3] recorded the noise from a 400kW wind turbine at a distance of 30m. From these measurements he concluded that the amplitude modulation is dominant in the frequency band between 1 kHz to 2 kHz and that the modulation is not related to the periodic blade passing by the tower. Van den Berg [4] reported that in a residential area close to a wind

farm whose residents complained about the amplitude modulation of wind turbine noise, the noise in daytime was only perceivable within a few hundred meters from the wind turbine. At night, however, he reported a periodic 'thumping' at distances of more than 1km from the wind farm, which he described as being more impulsive in character compared to swishing noise. He attributed this difference to the stable atmospheric conditions prevailing at night. Bowdler [5] investigated the effects of vertical and horizontal wind shear on the relative level of turbine noise and background noise. He also examined differences in wind speeds and wind directions in the vicinity of the blade tip trajectory that might cause excessive amplitude modulation. Lenchine [6] has also measured the noise due to a modern wind turbine generator, focussing on the influence of amplitude modulation on noise perception. Napoli [7] carried out a case study of noise measurement for a pitch-regulated variable speed wind turbine that was known to cause numerous complaints from nearby residents. He measured the sound power level and far field sound pressure levels with emphasis on quantifying the impulsive sounds during night time and downwind conditions.

To date, only a few studies have attempted to understand and predict in detail amplitude modulation of wind turbine noise. Oerlemans and Schepers [8] have analysed and characterized swishing noise using classical analytical flat plate trailing edge noise theory and semi-empirical radiations models originally developed for rotor and propeller noise prediction. Predictions from their semi-empirical model were shown to be in good agreement with measurements of the wind turbine noise frequency spectrum. The model also predicts the variation in noise at a fixed observer position as the blades rotate thereby providing an estimate for the degree and characteristic of the swishing noise. They attribute the cause of swishing noise to cyclic variations in trailing edge noise directivity and convective amplification. In view of the importance of swishing noise in affecting the acceptance of wind turbine to communities living close by a better understanding of its character and mechanisms is needed.

This paper describes a new approach to analyzing and predicting the swishing sound generated by wind turbines. This method allows the origins of its time frequency spectrum to be separated due to the airfoil broadband noise in a steady mean flow and the source rotation effects, thereby elucidating the main causes of the wind turbine amplitude modulation. The analysis method exploits the property that the statistics of the noise signal from the wind turbine vary periodically with time, a property referred to as cyclostationarity. Cyclostationary theory was developed initially for telecommunications applications in which the data are modulated by a carrying sinusoidal signal. Cyclostationary spectral analysis has also been applied to many mechanical systems involving rotating elements by Antoni et al. [9] and Bonnardot et al. [10], and to several aerodynamic problems to characterize unsteady time/space periodic turbulent flows by Jurdic et al [11]. In aeroacoustic applications only helicopter noise signals [12] appear to have been investigated using this method.

Our prediction approach is based on the Amiet's model [14, 15] for propeller trailing-edge noise, which is ideally suited to the prediction of wind turbine noise since it based on the notion of instantaneous spectrum, although Amiet never explicitly recognized this property. In essence the propeller noise is predicted from the average of the noise over all blade positions based on the assumption that the noise at any blade position is identical to that as if the blade is locally translating. The prediction of the broadband noise from rotating blade is of great interest in many

industrial applications, aircraft propeller noise, helicopter noise, cooling fan noise as well as wind turbine noise. Since the first general model for broadband noise predictions from rotating blades developed by Ffowcs Williams and Hawkings [16], many empirical and semi-analytical models [17-19] have been subsequently developed. To deal with the computational cost associated with the use of these models, which was considered high at the time, Amiet [20] proposed a simplified alternative approach, which has been widely used since. Recently, Blandeau and Joseph [15] have made an extensive investigation into the validity of the classical model by Amiet by comparing this approximate model with an exact model in which the effects of rotation are treated exactly. Mean flow effects were neglected, however, and their comparisons are only valid at low tip speed Mach numbers. They showed that Amiet's model exhibits excellent agreement with the exact model, especially for wind turbine noise, where the rotation period is much less than the period at audio frequencies. A more general analysis is presented by Sinyaoko et al. [21].

Cyclostationary theory is outlined in Section 2. Cyclostationary analysis is then applied to the noise signals measured close to an upwind axial-type 1.5 MW wind turbine. In Section 5, Amiet's model for rotor trailing-edge noise is extended and expressed in a form to allow direct comparison with cyclostationary noise measurements. In Section 7 we define and quantify a swishing index as a single measure of the swishing character of wind turbine noise.

2. Cyclostationary Theory

Assuming identical blades the statistics of the noise signal from a wind turbine will vary in time periodically. Any random signal with this periodicity property is classified as cyclostationary. The period of the statistical characteristics is called the cycle *T*. The statistical estimators for cyclostationary signals are applied in this paper to the measured wind turbine noise signals. An extensive review of the cyclostationary theory and its applications have been presented by Gardner et al. [13] and more recently by Jurdic & Joseph [11] whose main results we now review.

2.1 The coherent average

For a cyclostationary process, the ergodicity assumption in which the ensemble-average operator $\mathbb{E}\{\}$ can be replaced by the time-average operator is not appropriate because the time average and ensemble average will give different results. However, Boyles and Gardner [22] have extended the ergodicity principle to define the notion of cycloergodicity for a cyclostationary process. The ensemble average is therefore replaced by a cycle average defined by, for example, Braun [23] who has introduced the cycle average operator to estimate the ensemble-average in the form:

$$\mathbb{E}\{p(t)\} = \lim_{K\to\infty} \frac{1}{K}\sum_{k=0}^{K} p(t+kT) \qquad (1)$$

2.2 Second-Order Moments

The 'power' distribution of a cyclostationary signal is characterized by its various second-order moments, whose definitions in terms of acoustic pressure *p(t)* are given below.

A. Autocorrelation Function

The autocorrelation function quantifies the dependence of a signal at a moment in time *t* to the signal at a time τ later (or before), defined by,

$$\mathcal{R}_{pp}(t,\tau) = \mathbb{E}\left\{p\left(t+\frac{1}{2}\tau\right)p^*\left(t-\frac{1}{2}\tau\right)\right\} \qquad (2)$$

For cyclostationary signals the autocorrelation function has the periodicity property,

$$\mathcal{R}_{pp}(t+kT,\tau) = \mathcal{R}_{pp}(t,\tau). \qquad (3)$$

B. Cyclic Autocorrelation function

One of the most useful aspects of the periodicity property in Eq. (3) is that the autocorrelation function can be expressed as the Fourier series expansion

$$\mathcal{R}_{pp}(t,\tau) = \sum_{\alpha_j} \mathcal{R}_{pp,\alpha_j}(\tau)\mathrm{e}^{i2\pi\alpha_j t} \qquad (4)$$

where $\alpha_j = j/T$, *j* being an integer. Since the Fourier coefficients $\mathcal{R}_{pp,\alpha_j}$ are only a function of τ they are referred to as the cyclic autocorrelation or cyclocorrelation function and may be deduced by the inversion of Eq. (4),

$$\mathcal{R}_{pp,\alpha_j}(\tau) = \frac{1}{\mathrm{T}}\int_{-\mathrm{T}/2}^{\mathrm{T}/2} \mathcal{R}_{pp}(t,\tau)\mathrm{e}^{-i2\pi\alpha_j t}\,\mathrm{dt} \qquad (5)$$

Equation (5) forms the basis of the method used here for characterizing the periodic variation in broadband noise referred to as swishing.

C. Spectral Correlation

Measurements of the noise radiated from wind turbines are often presented in the frequency domain to quantify its spectral content. For a stationary signal, the Fourier transform over τ of the autocorrelation function of Eq. (2) yields the power frequency spectrum. In the case of a cyclostationary process, the autocorrelation function depends on the time *t* and the time lag τ. The Fourier transforms over these parameters *t* and τ define the spectral correlation function $\mathcal{SC}_{\mathrm{pp}}$:

$$\mathcal{SC}_{pp}(\alpha,f) = \int_{-\infty}^{\infty}\int_{-\infty}^{\infty} \mathcal{R}_{pp}(t,\tau)\mathrm{e}^{-i2\pi\alpha t}\mathrm{e}^{-i2\pi f\tau}\,\mathrm{dt}\mathrm{d}\tau \qquad (6)$$

Equation (6) characterizes the power distribution versus spectral frequency *f* for each discrete

cyclic frequency component α. The variation with α quantifies the frequency components of the energy distribution of the cyclostationary signal $p(t)$ during the cycle *T*, i.e., the swishing sound of wind turbines. Another interpretation of $\mathcal{SC}_{pp}$ is that it represents the frequency domain correlation function

$$\mathcal{SC}_{pp}(\alpha, f) = \lim_{T\to\infty} \frac{1}{T} \mathbb{E}\left\{P_T\left(f+\frac{1}{2}\alpha\right) P_T^*\left(f-\frac{1}{2}\alpha\right)\right\} \qquad (7)$$

where $P_T(f)$ is the short-time Fourier transformation of *p(t)* over large but finite duration *T*:

$$P_T(f) = \int_{-T/2}^{T/2} p(t)\, e^{-i2\pi f t} dt \qquad (8)$$

D. Cyclic Power Spectrum

Substitution of Eq. (4) into Eq. (6) leads to,

$$\mathcal{SC}_{pp}(\alpha, f) = \sum_{\alpha_j} S_{pp,\alpha_j}(f)\delta(\alpha - \alpha_j) \qquad (9)$$

where δ is the Dirac delta function. The spectral correlation is therefore discrete in α - frequency and continuous in the spectral frequency *f*:

Substituting $j = 0$ in Eq. (7) and (9) suggests that the cyclic power spectrum is equal to the power spectrum $S_{pp}(f)$ for stationary signals, i.e., $S_{pp,\alpha_0}(f) = S_{pp}(f)$. The cyclic power spectrum can also be defined in terms of the Fourier transform of the cyclic autocorrelation function

$$S_{pp,\alpha_j}(f) = \int_{-\infty}^{\infty} \mathcal{R}_{pp,\alpha_j}(\tau) e^{-i2\pi f \tau} d\tau \qquad (10)$$

E. Wigner-Ville Spectrum

The Wigner-Ville spectrum has been defined as the unique Generalized spectrum for time-varying spectral analysis [24]. For a non-stationary process, the Wigner-Ville spectrum $\mathcal{WV}_{pp}(t, f)$ is utilized to quantify the instantaneous power spectrum of the signal at time *t*. It can be obtained either by Fourier transformation of the autocorrelation function $\mathcal{R}_{pp}$,

$$\mathcal{WV}_{pp}(t, f) = \int_{-\infty}^{\infty} \mathcal{R}_{pp}(t, \tau)\, e^{-i2\pi f \tau} d\tau \qquad (11)$$

or by the inverse Fourier series of the cyclic power spectrum S_{pp,α_j} by

$$\mathcal{WV}_{pp}(t,f) = \sum_{j=-\infty}^{\infty} S_{pp,\alpha_j}(f) e^{i2\pi\alpha_j t} \qquad (12)$$

F. Instantaneous Variance

In the case of stationary signals, its variance quantifies the energy of the signal and, for zero-mean signals, it is defined as the mean square value of *p(t)*:

$$\overline{p^2} = \mathbb{E}\{p^2(t)\} = \mathcal{R}_{pp}(0) = \int_{-\infty}^{\infty} S_{pp}(f)\mathrm{d}f \qquad (13)$$

For cyclostationary signals $p(t)$, the instantaneous variance can be defined to quantify the variation of the mean square acoustic pressure over the cycle;

$$\overline{p^2}(t) = \mathcal{R}_{pp}(t,0) = \int_{-\infty}^{\infty} \mathcal{WV}_{pp}(t,f)\mathrm{d}f \qquad (14)$$

In the present application, $\overline{p^2(t)}$ in the far field is proportional to the sound intensity variation. From Eqs. (3) and (14), $\overline{p^2(t)} = \overline{p^2(t+kT)}$.

Finally, the variance $\overline{p_{\alpha_j}^2}$ of each cyclic component α_j can be computed from

$$\overline{p_{\alpha_j}^2} = \int_{-\infty}^{\infty} \mathcal{SC}_{pp}(\alpha_j, f)\mathrm{d}f \qquad (15)$$

This quantity, $\overline{p_{\alpha_j}^2}$, will be subsequently used to define a 'swishing index' that provides a single metric of the extent of swishing.

3. Wind Turbine Noise Measurements

Cyclostationary spectral analysis is now applied to the acoustic pressure measured in the close vicinity of a large modern upwind wind turbine where swishing noise was clearly discernible. The noise measurements were carried out at the Hankyung wind farms on Jeju Island [25, 26] in South Korea. The Hankyung wind farm is composed of four WTs with 1.5 MW capacities, and three recently installed WTs with 2 MW capacities, which were not present at the time of measurement. The wind turbine under investigation was selected as it is furthest from the neighboring wind turbines. The third wind turbine of 1.5 MW capacity located in the easternmost area of the Hankyung wind farm was examined. Detailed specifications are given in Table 1.

Table 1. Specification of a target wind turbine at Hankyung wind farm.

Rated Output	1.5 MW
Rated Wind Speed	15 m/s
Rotor Diameter	72 m
Tower Height	62 m
Operating Wind Speeds	4-25 m/s
Rotor Speed	17.3 rpm
Power Regulation	Active Stall
Annual Generation	3,343 MWh (Vmean = 6.5 m/s)

Measurement instrumentation and procedures based on the IEC61400-11 (2002) standard were used to evaluate the noise emission from the turbines. Additional noise measurements were also taken 10m downstream of the wind turbine. Noise measurements were made using a microphone positioned on a circular rigid board placed on the ground to reduce wind noise generated at the microphone, and to minimize the influence due to variations in the soil type. Acoustic data from the microphones were recorded on digital audio tape at a sampling frequency of 24 kHz. Wind speeds at 10m above ground were measured at the same time as the noise measurements in accordance with the IEC61400-11 standard. A mobile meteorology mast was positioned at this height to measure the wind speed, wind direction, and other atmospheric conditions. More detailed information about the measurement is provided in references [25, 26].

4. Cyclostationary Analysis

The cyclostationary analysis described in Section 3 requires the cycle time T to be known a priori. The obvious choice for T is the time taken to complete one rotation of the wind turbine. Another equally reasonable choice, particularly when th9)ere are no significant blade–to-blade differences, is the time taken between successive blade arrivals T_{bpf}. The noise data was collected at a sampling frequency of F_s = 24kHz. The rotation speed of the turbine was 17.3 rpm such that each blade passage is represented by 27746 samples, corresponding to a time interval of 1.156 s. This will be the assumed periodicity of the noise statistics in the analysis presented below. Each measurement was acquired for appropriately 25s. The cyclostationary analysis results presented in this paper are therefore based on the average of K=21 cycles, corresponding to 7 rotations (for the three bladed wind turbine). The total acquisition time was chosen to ensure that the variation in wind speed over the measurements period was a minimum.

4.1 Measured Acoustic Pressure Signals and Stationary Analysis

Figure 1 shows a typical acoustic pressure time history *p(t)* of 25s duration.

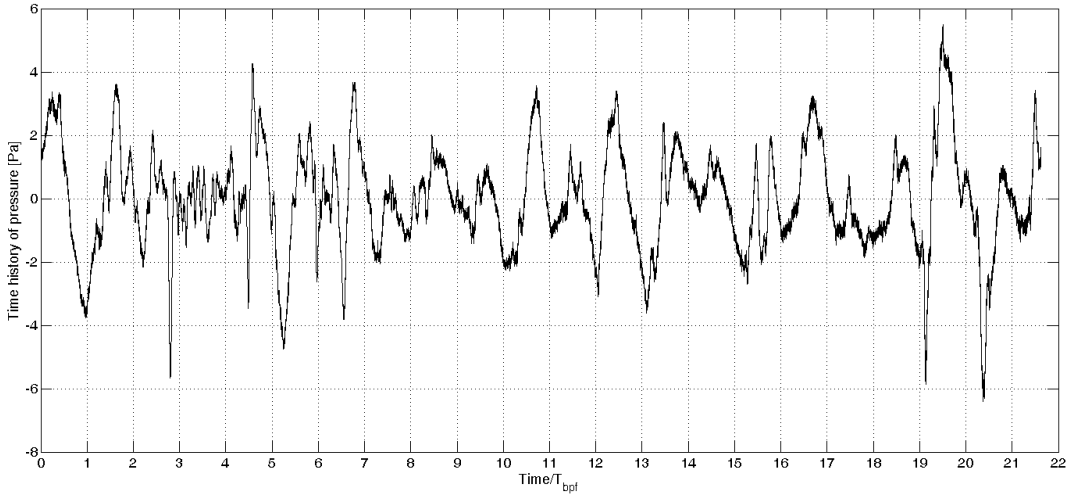

Fig. 1 Time history of measured acoustic pressure

The periodic behavior in the measured acoustic signal at the blade passing frequency at about 1Hz is seen to be obscured by random pressure fluctuations. Before undertaking cylcostationary analysis of the measured signal, a conventional spectrum was obtained (i.e., with stationarity assumed) from the entire 25s time series in order to extract the general behavior of the averaged spectrum. This measurement obtained assuming stationarity will be shown in Section 5 to be identical to the cyclostationary spectrum for j = 0, as explained above. The power spectral density obtained with assumed stationarity is plotted in Fig. 2. Figure 2a shows the spectrum plotted on a linear frequency scale while 2b is plotted on a logarithmic scale at frequencies below about 1,750Hz.

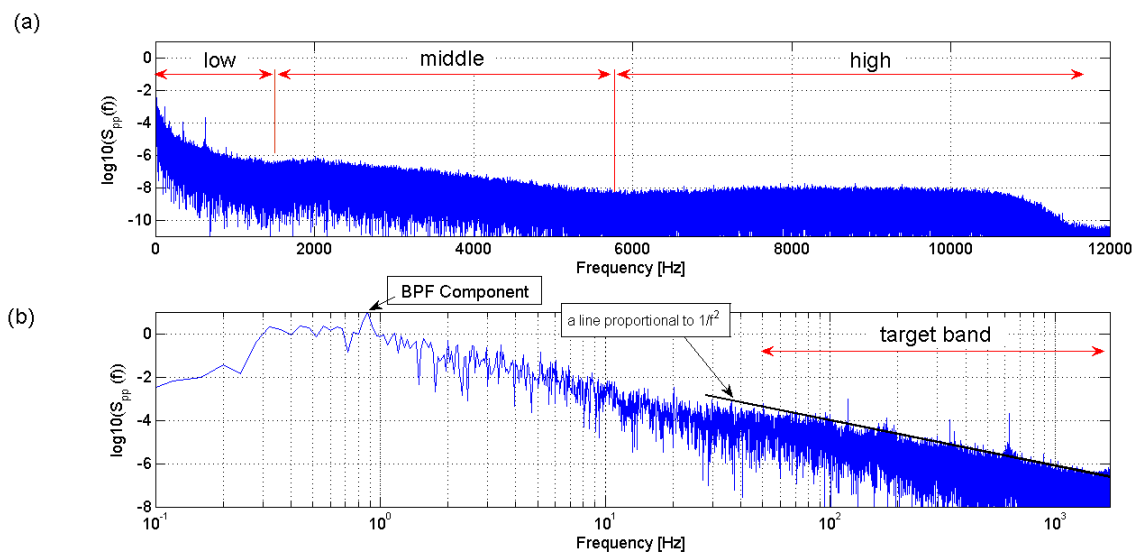

Fig. 2 Power spectral density of *p(t)*: (a) over whole frequency range and (b) over the zoomed frequency range

The spectrum in Fig. 2a reveals three distinctive frequency ranges; low (f < 1750 Hz),

intermediate (1750 Hz < f < 5500 Hz) and high (f > 5500Hz). Each frequency region is characterized by different frequency decay laws. The reason for these differences is presently not known but may be due to different noise generation mechanisms. However, as the absolute levels in the low frequency range are much greater than those in intermediate and high frequency ranges, the overall time variation in sound pressure levels is dominated by this low frequency region.

Fig. 2b shows the spectrum of Fig. 2a in the frequency range below 1750 Hz plotted on a logarithmic frequency scale. Two distinctive bandwidths in the spectrum can now be seen, above and below about 30-50 Hz. The spectrum in the lower frequency range comprises numerous tonal noise components where the maximum amplitude is identified at the blade passing frequency of 0.865 Hz, although high harmonics of the BPF are difficult to identify. Due to the very low rotational speeds of modern large axial wind turbines, these tonal noise components generally lie in the infrasound part of the noise spectrum, which dominate the behavior of the acoustic pressure time signal shown in Fig. 1. Figure 3 shows the variation in the pressure signal in Figure 1 versus time normalized on the blade passage period after being high-pass filtered above 50 Hz. The periodicity in the signal that characterized swishing noise is now more clearly revealed.

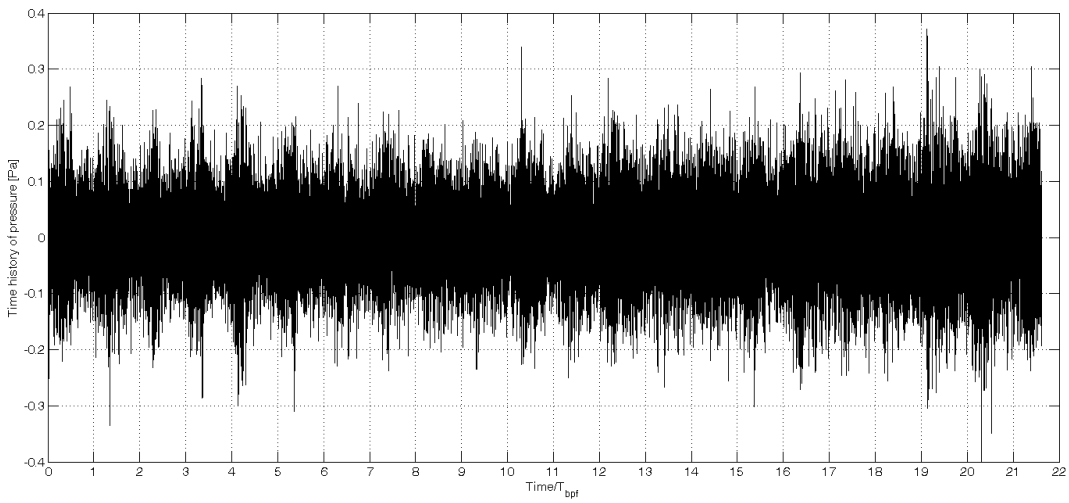

Fig. 3 High-passed filtered time signal of acoustic pressure over 50 Hz

4.2 Cyclostationary Analysis

One useful representation of the swishing character of the wind turbine is the time variation of the frequency spectrum. This information may be deduced from the Wigner-Ville spectrum applied to the fluctuating acoustic pressure. The results are plotted in Fig. 4 over one blade passage period versus blade angle evaluated at observer time. In Fig. 4, the Wigner-Ville spectrum has been estimated assuming a cycle duration of $T = T_{bpf}$ to reveal the time evolution of the noise spectrum and hence reveal the characteristics of the swishing noise. The time evolution of the spectrum shown in Figure 4 may be split into three frequency bandwidths.

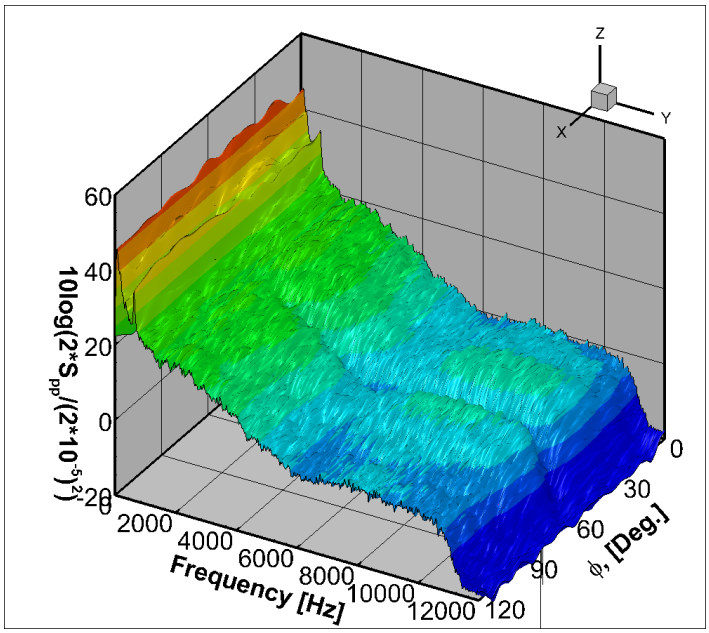

Fig. 4 Wigner-Ville spectrum applied to the measure pressure fluctuation

In the frequency range above about 1750 Hz, the spectrum exhibits a peak in the level at blade angles of approximately 40 and 85 degs (evaluated at observer time) with a dip in the spectrum at angles in between. The physical interpretation of these angles will be made clearer through comparison with predictions in Section 6. The temporal variation of the mean squared pressure obtained by integrating the data in Fig. 4 over each frequency band identified in Fig. 2 is plotted in Fig. 5.

Figures 5a and 5b show the time-variation of sound pressure levels averaged over the entire frequency range and when averaged over the lower frequency band, 20 Hz – 1750 Hz, respectively. The cyclic level variation in this band can be seen to match the variation in the overall behavior of time-variation of acoustic pressure, suggesting that the overall swishing property is determined by the noise in this frequency range. Figures 5c and 5d show the time-variations of sound pressure in the frequency band, 1750 Hz – 5500 Hz and 5500 Hz – 12000 Hz, respectively. Two peaks in the time history can be identified in both figures. These peaks are analyzed in detail in Section 6 and shown to be related to the cyclic variation in the unsteady blade loading function. These peaks are observed to become weaker as frequency decreases.

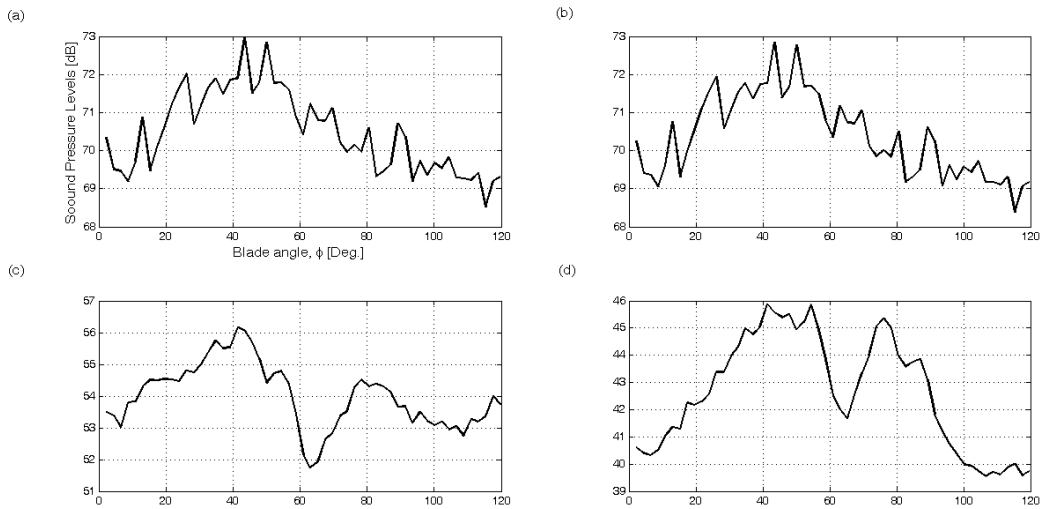

Fig. 5. Time-variation of sound pressure levels : (a) over entire frequency range, (b) in lower frequency band (20 – 1750 Hz), (c) intermediate frequency band (1750 – 5500 Hz), and (d) higher frequency band (5500 – 12000Hz)

The spectra in the three bandwidths identified in Fig. 2 follow a different frequency power-law, which suggests that different noise generation mechanism may be present in each frequency bandwidth. This issue will not be investigated further in this paper since our main focus is on the investigation of swishing noise.

The magnitude of the acoustic pressure spectral correlation $|SC_{pp}\ (\alpha_j, f)|$ is plotted in Fig. 6 versus the BPF cyclic order. Note that the cyclic spectrum is symmetric in α, such that $SC_{pp}\ (-\alpha_j, f) = SC_{pp}\ (\alpha_j, f)$. It can be seen that the stationary cyclic power spectrum corresponding to $\alpha_j = 0$ is almost identical to the spectrum shown in Fig. 2 computed with stationarity assumed. Small differences present are due to the different frequency resolution in the two cases. Assuming that the noise statistics is stationary in the rotating reference frame, swishing noise is therefore solely an artifact of source rotation, which is quantified by the cyclic power spectra for $\alpha_j \neq 0$. Figure 6 shows the various cyclic power spectra of non-zero cyclic order to be similar to the spectrum obtained using conventional spectral analysis (i.e., for j = 0) applied to the entire 25s time series. This is because the cyclic (blade-passing) period is very long compared with a typical acoustic time period.

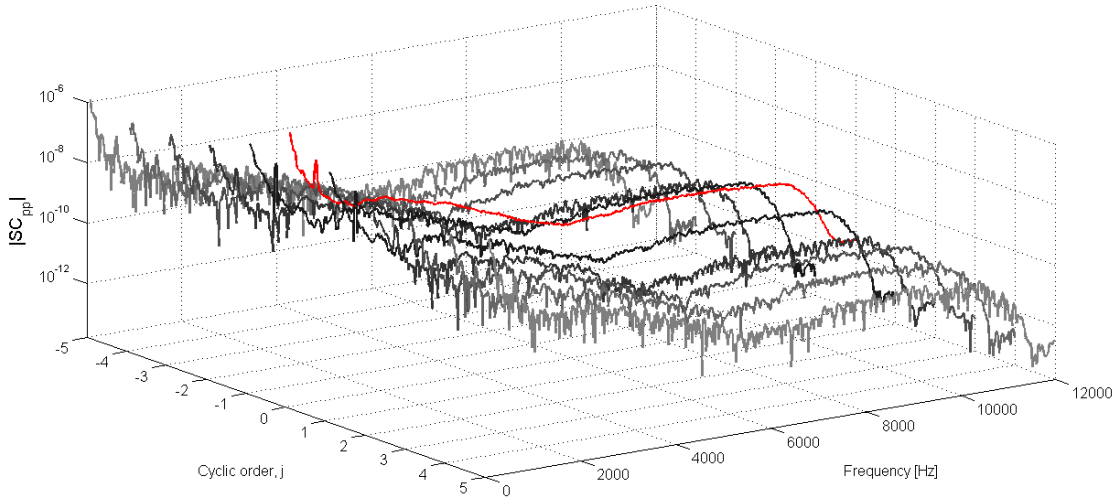

Fig. 6 Cyclic power spectra for various values of α_j for $j = -5{:}5$.

In Fig. 7, the cyclic power spectra non-dimensionalized by $\overline{p_{\alpha_j}^2}$ defined by Eq. (15), are plotted for different values of j. Relatively good collapse of the spectra is obtained, although there is a small difference in level at frequencies above about 1750 Hz.

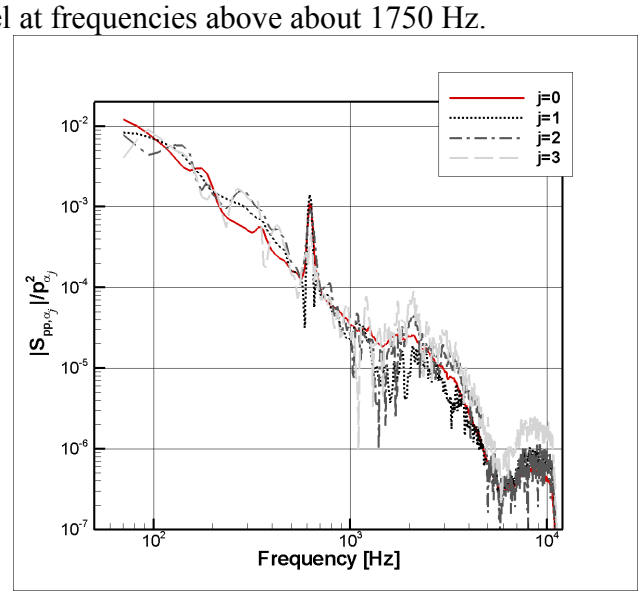

Fig. 7 Normalized cyclic power spectra for the cyclic orders=0:3

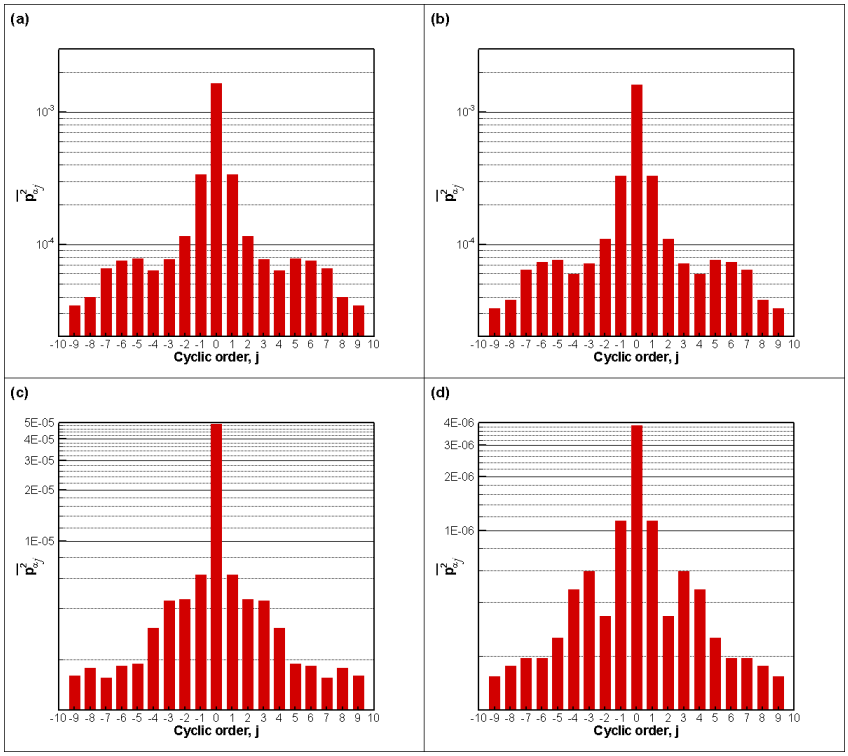

Fig. 8 Cyclic-spectral distribution of the instantaneous acoustic power of the measured pressure *p(t)* (a) over the entire frequency range, (b) in the lower frequency band, (c) in the middle frequency band, and (d) in the higher frequency band.

Figure 8 presents cyclic spectral distributions $\overline{p^2_{\alpha_j}}$ of the acoustic power versus cyclic order evaluated over the entire frequency range and in each frequency band. As already observed in Fig. 5, differing behaviors are observed in each of the three frequency bandwidths suggesting a different degree of swishing in each bandwidth. The cause of this difference in the α – spectra across the three frequency bands is presently unclear but may be a consequence of the different noise generation mechanisms in each frequency band. The cyclic-spectral distribution in the lowest frequency band can be also seen to match the overall distribution, suggesting again that the overall noise variation is dominated by low frequency noise.

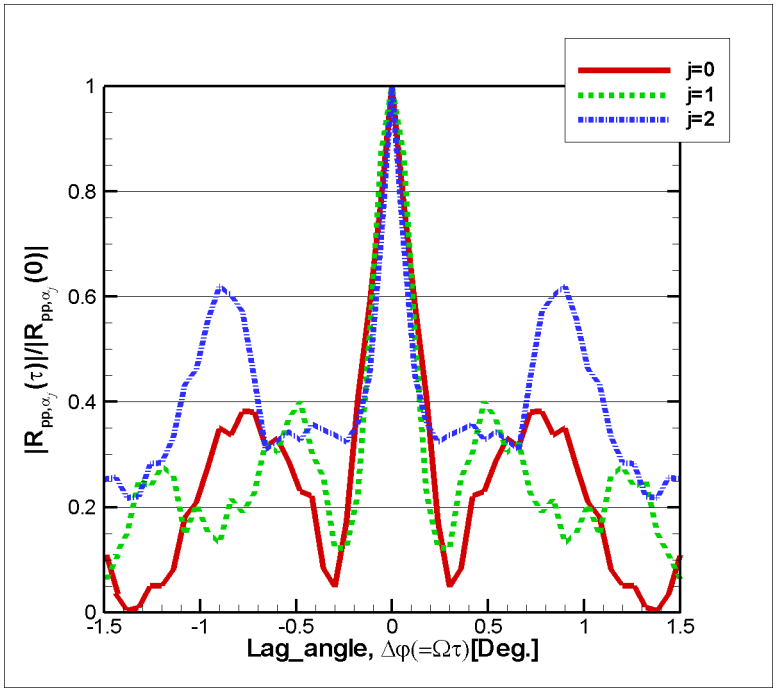

Fig. 9 Normalized cyclic autocorrelation function for various values of α_j.

Figure 9 shows the cyclic autocorrelation functions defined in Eq. (4) normalized by its peak value at zero lag angle for various values of α_j up to *j=2* over the entire frequency range. The cyclic autocorrelation functions collapse reasonably well in the vicinity of $\Delta\varphi = 0°$ $(\tau = 0s)$, which is consistent with the collapse of the cyclic spectra shown in Fig. 7.

The width of the cyclic correlation functions in Fig. 9 provides information about the characteristic time scale of wind turbine noise. This dependence will be explored in further detail in Section 6 where the measurements are compared with predictions. Good collapse of the cyclic autocorrelation functions in Fig. 9 suggests that the length-scale is independent of the cyclic order and is therefore related to the noise generation mechanism and not to the effects of source rotation.

The instantaneous autocorrelation function $R_{pp}(t,\tau)$, obtained by the inverse Fourier transform of the Wigner-Wille spectrum with respect to *f*, is plotted in Fig. 10 for a single blade-passing period. Note that, for zero lag angle $(\varphi = 0)$, $R_{pp}(t,0)$ corresponds to the instantaneous mean square pressure.

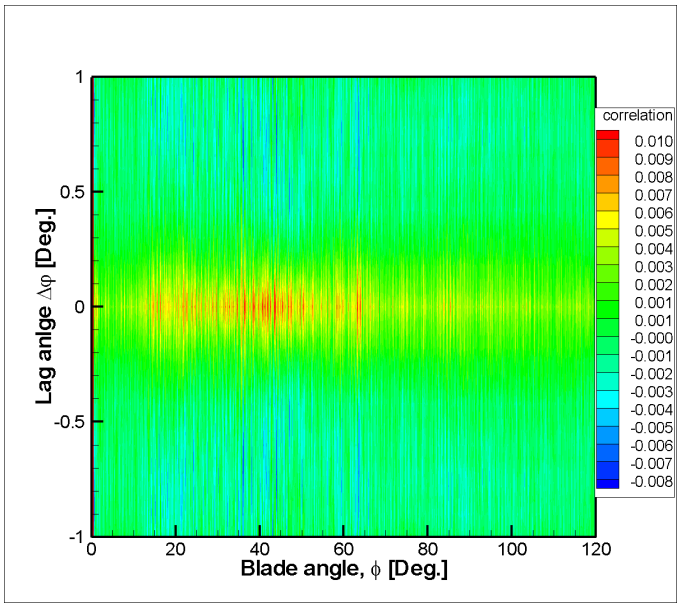

Fig. 10 Instantaneous autocorrelation of the measured acoustic pressure

5. Instantaneous spectrum derived from Amiet's Model for Propeller Trailing Edge Noise

In this section the analytical formulation due to Amiet for the radiated broadband trailing edge noise due to rotating propellers is used to develop an expression for the noise spectrum at any instant in time corresponding to a particular blade position. The conventional time-stationary spectrum then follows from the average over all such contributions taken over a complete blade rotation. The analysis of Amiet's method presented by Blandeau and Joseph [15] is corrected and extended in a form to facilitate noise predictions that allow comparison with the noise data obtained from cyclostationary analysis. In Amiet's original model, the spectrum is obtained from average over all blade positions and hence the radiated noise was predicted to be axis-symmetric with no dependence on observer azimuthal position ψ_0. In this study, we are concerned with the temporal variability in spectra, which will be shown to have a strong azimuthal dependence by virtue of the time varying source strength and propagation path.

The starting point of Amiet's model is the observation made by Lowson [27] that the effect of the rotation on rotor noise is negligible when the angular frequency of rotation is very small compared to the angular acoustic frequency, i.e. $\omega/\Omega \gg 1.$ This model for the self noise of a rotor treats the effects of rotation as a series of translations over an infinitesimal distance.

Amiet's model was shown to have broader validity by Blandeau and Joseph [15] by obtaining good agreement with the exact solution over a much higher frequency range than suggested by the condition above. For a wind turbine Amiet's approach was shown to be accurate over most of

the audio frequency range.

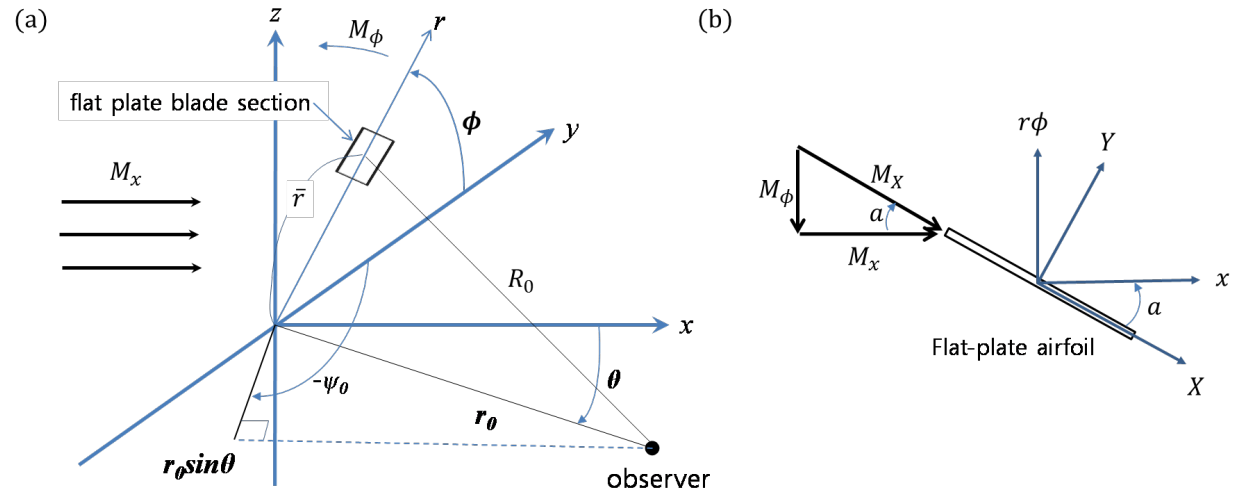

Fig. 11 Coordinate systems defining the locations of a blade section and observer: (a) propeller coordinates and (b) airfoil-bound coordinates

Figure 11 shows the coordinate systems describing the position of a blade section, represented by a flat plate. The location of an observer with respect to the center of a *B*-bladed rotor can be expressed in the spherical coordinate system (r_0, θ, ψ_0) or in the Cartesian coordinate system (x, y, z). The location of the blade can be expressed in the cylindrical coordinate system (r, ϕ, x) or in the airfoil-bound Cartesian coordinate (r, X, Y), both centered at the midchord of the airfoil. The relation between the airfoil-bound coordinates $[(r-\bar{r}), X, Y]$ and the polar observer coordinate (r_0, θ, ψ_0), which include the effect of blade stagger angle a and azimuthal angle ϕ, can be obtained from

$$\begin{bmatrix} r-\bar{r} \\ X \\ Y \end{bmatrix} = \mathcal{T}_a \mathcal{T}_\phi \begin{bmatrix} r_0 \cos\theta \\ r_0 \sin\theta \cos\psi_0 \\ r_0 \sin\theta \sin\psi_0 \end{bmatrix} - \begin{bmatrix} \bar{r} \\ 0 \\ 0 \end{bmatrix} \tag{16}$$

where $\mathcal{T}_a$ and $\mathcal{T}_\phi$ are rotation matrices defined by

$$\mathcal{T}_\alpha = \begin{bmatrix} 1 & 0 & 0 \\ 0 & -\sin\alpha & \cos\alpha \\ 0 & \cos\alpha & \sin\alpha \end{bmatrix}, \ and \ \mathcal{T}_\phi = \begin{bmatrix} 0 & \cos\phi & \sin\phi \\ 0 & -\sin\phi & \cos\phi \\ 1 & 0 & 0 \end{bmatrix} \qquad (17)$$

The azimuthal Mach number of the blade section is M_ϕ and the wind speed axial Mach number denoted by M_x. The wind speed is assumed to be constant over the circular path of a blade segment for simplicity. Note that the wind speed variation over the path affects the swishing sound and needs to be modeled if the related parameters are known. In Amiet's model described below, strip theory is used in order to represent the spanwise variation of the aerodynamic parameters and geometry. For simplicity we confine our attention to a single strip of width Δr centered at radius $\bar{r}$.

The relation between the observer time *t* and the source time t' can be expressed in the form,

$$t = t' + \frac{R_0}{c_0} \qquad (18)$$

where $R_0 = \sqrt{(r-\bar{r})^2 + X^2 + Y^2}$ is the distance between the observer and the source at the time t'. The effect of the wind velocity is neglected in Eq. (18). Observer and source times in Eq. (18) can be converted into the blade position angle ϕ by multiplication by the angular rotation speed Ω. Equation (18) leads to

$$\phi_t = \phi_{t'} + \Omega\frac{R_0}{c_0} \qquad (19)$$

where $\phi_t = \Omega t$ and $\phi_{t'} = \Omega t'$ are the blade position angles at the receiver and source time, respectively.

Amiet introduces the Doppler factor below to take into consideration the relative movement of a rotating blade segment alternatively away from and toward the observer in far field. Based on the coordinate systems for the moving source and the observer in Fig. 11, the Doppler-shifted

frequency ω for the observer at (r_0, θ, ψ_0) can be derived in the form. ,

$$\omega = D_p \omega_\phi \qquad (20)$$

where ω_ϕ is the source frequency observed in the rotating reference frame, D_p is the inverse Doppler factor defined as

$$D_p = \frac{1}{1 - M_{\phi R_0}} . \qquad (21)$$

Here, $M_{\phi R_0}$ is the Mach number component of the source velocity in the direction of the observer, defined by

$$M_{\phi R_0} = \frac{r_0}{R_0} M_\phi \sin(\psi_0 - \phi) \, sin\theta \qquad (22)$$

where $M_\phi = \bar{r}\Omega / c_0$ is the rotation Mach number. Note that Eq. (22) is valid for observers both in the near field and far field. For far field observers Eq. (22) simplifies to $M_{\phi R} = M_\phi \sin(\phi - \psi_0) sin\theta$. Evaluating the Power Spectral Density (PSD) from the Fourier transform of the autocorrelation function demonstrates that the time-frequency pressure PSD at observer position (r_0, θ, ψ_0) due to a rotating blade section at location ($\bar{r}$, ϕ_{tr}, 0) can be written as, for example, Sinayoko [21]

$$S_{pp,Amiet}(r_0, \theta, \psi_0, \omega, \phi_t) = \left(\frac{\omega_{\phi_{tr}}}{\omega}\right) S_{pp,\phi_{tr}}(r_0, \theta, \psi_0, \omega_{\phi_{tr}}) \qquad (23)$$

where the blade position is evaluated at the source time. The term $S_{pp,\phi_{tr}}$ in Eq. (23) corresponds to the PSD of the trailing-edge noise due to a translating rectangular blade segment centered at a radius $\bar{r}$. It can be expressed in the airfoil-bound coordinate system $(r - \bar{r}, X, Y)$ from [28, 29]

$$S_{pp,\phi_{tr}}(r_0, \theta, \psi_0, \omega_{\phi_{tr}}) = \frac{1}{2\pi}\left(\frac{\omega_{\phi_{tr}} cY}{2c_0 \sigma^2}\right)^2 \Delta r \left|\mathcal{L}(k_{r,\phi_{tr}}, K_{X,\phi_{tr}}, \kappa_{\phi_{tr}})\right|^2 S_{qq}(k_{r,\phi_{tr}}, K_{X,\phi_{tr}}) \qquad (24)$$

where $\sigma^2 = X^2 + \beta_X^2[(r-\bar{r})^2 + Y^2]$, and $\beta_X = \sqrt{1-M_X^2}$. The span-wise and chordwise turbulence wavenumbers and the aeroacoutic coupling wavenumber are, respectively, given by

$$k_{r,\phi_{t'}} = \frac{\omega_{\phi_{t'}}}{U_c}\frac{r-\bar{r}}{\sigma}, \qquad K_{X,\phi_{t'}} = \frac{\omega_{\phi_{t'}}}{U_c} \quad \text{and} \quad \kappa_{\phi_{t'}} = \frac{k_0}{\beta_X^2}\left(M_X - \frac{X}{\sigma}\right) \tag{25}$$

The final expression for the PSD due to the blade section at position $(\bar{r}, \phi_{t'}, 0)$ expressed in a polar observer coordinate, as predicted using Amiet's approach, can therefore be obtained by substituting Eqs. (16-17) and Eqs. (24) into (23) to give

$$S_{pp}(r_0,\theta,\psi_0,\omega,\phi_t)$$

$$= \frac{1}{2\pi}\left(\frac{\omega_{\phi_{t'}}}{\omega}\right)\left(\frac{\omega_{\phi_{t'}} c r_0}{2c_0\sigma^2}\right)^2 \Delta r D_{\phi_{t'}}(\theta,a,\psi_0)\left|\mathcal{L}(k_{r,\phi_{t'}},K_{X,\phi_{t'}},\kappa_{\phi_{t'}})\right|^2 S_{qq}(k_{r,\phi_{t'}},K_{X,\phi_{t'}}) \tag{26}$$

where

$$k_{r,\phi_{t'}} = \frac{\omega_{\phi_{t'}}}{U_c}\frac{r_0\sin\theta\cos(\phi_{t'}-\psi_0)-\bar{r}}{\sigma} \tag{27}$$

and

$$\kappa_{\phi_{t'}} = \frac{k_0}{\beta_X^2}\left(M_X - \frac{r_0}{\sigma}(\cos\theta\cos a + \sin\theta\sin a\sin(\phi_{t'}-\psi_0))\right) \tag{28}$$

The boundary layer convection velocity U_c can be related to the chordwise flow velocity by $U_c = 0.8U_x$ according to [28], and where D_ϕ is the directivity term

$$D_\phi(\theta,a,\psi_0) = (\cos\theta\sin a - \sin\theta\cos a\sin(\phi-\psi_0))^2 \tag{29}$$

The unsteady loading term $\mathcal{L}(k_r,k_x,\kappa)$ in Eq. (24) was derived by Roger and Moreau [30], who extended the earlier work of Amiet [28, 29] to consider the effects of skewed gusts and takes the form,

$$\mathcal{L}(k_r,k_x,\kappa) = \frac{e^{2i\Theta_2}}{i\Theta_2}\left\{e^{-2i\Theta_2}\sqrt{\frac{\Theta_1}{\Theta_1-\Theta_2}}\,\mathrm{erf}\left[\sqrt{2i(\Theta_1-\Theta_2)}\right] - \mathrm{erf}\left[\sqrt{2i\Theta_1}\right] + 1\right\} \tag{30}$$

where erf( ) is the Error function and where:

$$\begin{cases} \Theta_1 = \frac{c}{2} k_X + \mu_\infty + \mu M_X \\ \Theta_2 = \frac{c}{2}(k_X + \kappa) \end{cases} \quad (31)$$

Here, $\mu = \frac{k_X M_c c}{2\beta_X^2}, \mu_\infty = \sqrt{\mu^2 - \left(\frac{k_r c}{2\beta_X}\right)^2}$ for supercritical gusts and $\mu_\infty = -i\sqrt{\left(\frac{k_r c}{2\beta_X}\right)^2 - \mu^2}$ for subcritical gusts. Note that sub-critical gusts radiate weakly to the far field and there we confine the range of k_r included in the calculation to supercritical gusts.

The wavenumber cross spectrum of surface pressure S_{qq}, introduced in Eq. (26), is defined by, for example, Roger and Moreau [30] as

$$S_{qq}(k_r, k_X) = \frac{1}{\pi} l_r(k_r, k_X U_c) \Phi_{pp}(k_X U_c) \quad (32)$$

where Φ_{pp} is the PSD of the surface pressure close to the trailing edge, and where the spanwise correlation length is defined as

$$l_r(k_r, \omega) = \frac{U_c}{\omega} \frac{b_c}{b_c^2 \left(\frac{k_r \omega}{u_c}\right)^2 + 1} \quad (33)$$

where b_c is the inverse of exponential decay rate of the spanwise coherence function according to Brooks and Hodgson [31]. A typical value for b_c is 2.1. In this study, the semi-empirical model for Φ_{pp} due to Goody [32] is used and is given by

$$\frac{\Phi_{pp}(\omega) U_X}{\tau_w^2 \delta} = \frac{3.0\bar{\omega}^2}{(\bar{\omega}^{0.75} + 0.5)^{3.7} + (1.1 R_T^{-0.57} \bar{\omega})^7} \quad (34)$$

where $\tau_w = 0.5\rho_0 U_X^2 C_f$ is the wall shear stress, C_f is the friction coefficient, δ is the boundary-layer thickness, $\bar{\omega} = \omega\delta/U_X$ is the Strouhal number defined with respect the

boundary layer thickness, and R_T is the ratio of outer-to-inner timescales of the turbulence given by

$$R_T = (\delta/U_x)/(\nu/u_\tau^2) = \left(\frac{u_\tau \delta}{\nu}\right)\sqrt{\frac{C_f}{2}} \qquad (35)$$

6. **Comparison of Prediction with Measurement**

Predictions made using Eq. (26) for the variation in PSD with angular location of the blade section are compared with the cyclostationary measurements presented in Section 4. All predictions are made under the assumption that trailing edge noise is the dominant noise mechanism on the wind turbine [8,33]. However, the importance of inflow-turbulence for wind turbines noise remains to be determined, especially in the low frequency range. Swishing due to inflow turbulence noise may be treated using a similar approach to that presented here for self noise.

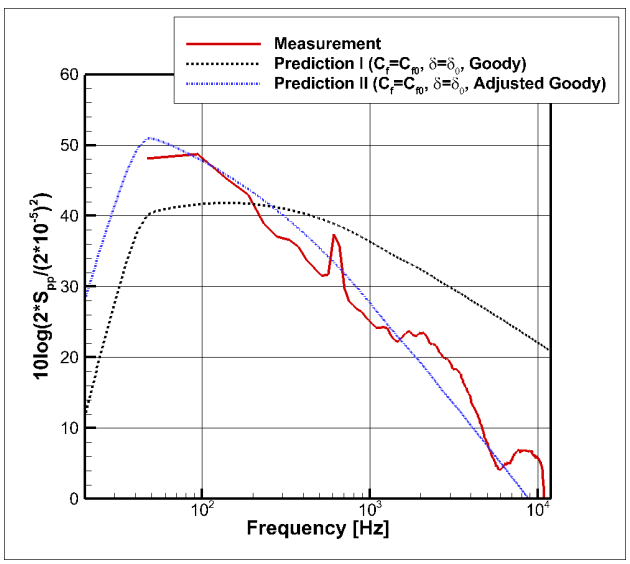

Fig. 12 Comparison of time-averaged PSD spectrum between the predictions and measurement

An initial comparison between the measured noise data with the time-averaged acoustic pressure PSD is presented in Fig. 12 using the original Goody model for the surface pressure spectral density. There blade segments of width $\Delta r = 30\ m$ are assumed to be located on the mean radius $\bar{r}$ equal to 70 % of the blade radius and seperated for each other by a ditance of $\Delta\phi = 120°$. Wind speed is assumed to be uniform across the blade rotating plane and equal to 14.79 m/s. Values for the friction coefficient of $C_{f0} = 0.00369$ and boundary layer thickness of

$\delta_0 = 0.073\ m$, were assumed in the expression for the surface pressure spectral density in Eq. (34). These values were deduced using the panel method code, XFOIL [34]. The instantaneous PSD at an observer time t in Eq. (26) is determined by interpolation between two neighbouring emission times t' for t in Eq. (19).

Reasonable agreement between the measured and predicted spectra are observed with the main difference being the rate at which the spectra decay with frequency, with the original prediction decaying more slowly with frequency than the measured spectrum. The overall shape of the predicted noise spectrum is principally determined by the choice of model for the surface pressure spectral density of Eq. (34). Numerous empirical (or semi-empirical) spectra to model turbulent boundary layer wall pressure spectra exist as reviewed by Blandeau [35]. We note that much better agreement with the measured noise data can be obtained by multiplying the Goody's surface pressure spectral density model by the factor, $2\bar{\omega}^{-1.5}$, as shown in Fig. 12. This modification of the Goody's model is arbitrary. Some recent works [36, 37] reported that the mean streamwise pressure gradient in the boundary layer significantly affects the wall pressure statistics and thus the wall-pressure models, such as the Goody's model, developed with the assumption of zero pressure gradient condition within the boundary layer may not be applicable in the present case. This is probably why a correction of Goody's model is needed to get the satisfactory agreement in Fig. 12. In addition, trailing-edge noise from wind turbines is known to involve both pressure-side and suction-side boundary layers, characterized by different parameters. The thicker suction-side boundary layer is suspected to dominate the middle frequency range, with a larger contribution of the pressure-side boundary layer at highest frequencies. However, all these aspects have not been retained in the present analysis because they are not expected to question the conclusions. Note that the predicted spectra are also high-pass-filtered at 50 Hz for consistency with the measurement. All subsequent comparisons are performed using Predictions II obtained from the adjusted Goody model.

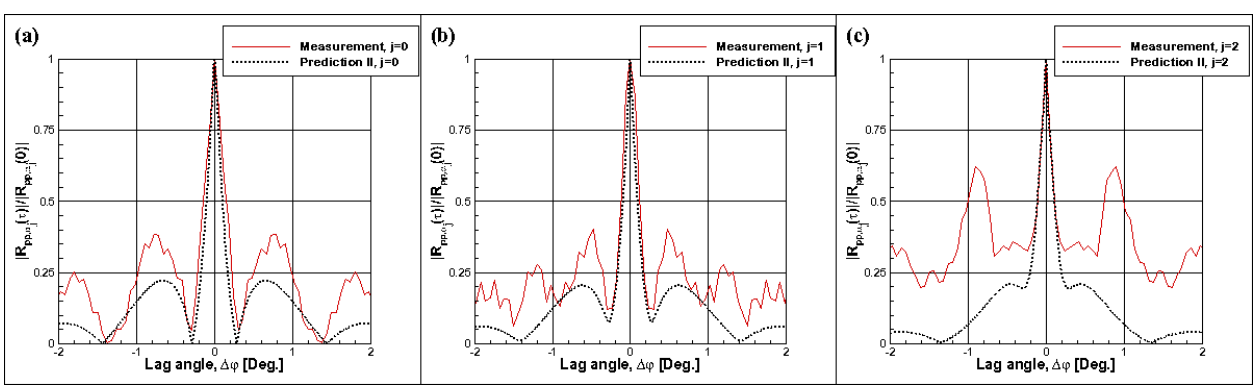

Fig. 13 Comparison of the normalized CAC between the prediction and measurement

Figure 13 shows a comparison between the predicted and measured cyclic auto correlation (CAC) for the cyclic orders j =0, 1 and 2. Each CAC is normalized by its maximum value at zero lag angle. The normalized CAC obtained using the adjusted Goody model shows good agreement with the measured CAC results. This can be attributed to the improved agreement in

the spectral decay rates shown in Fig. 12 since the effective bandwidth of the spectrum is smaller and hence the correlation bandwidth is larger. As discussed in Fig. 9, close agreement in the correlation bandwidth implies that the temporal length-scale (say, calculated from the value of τ_{half}, at which the cyclic autocorrelation function $\mathcal{R}_{pp,\alpha_j}(\tau)$ reaches half its maximum value of $\mathcal{R}_{pp,\alpha_j}(0)$) is the dominant length-scale involved in the noise generation, and hence its spectral and correlation characteristics, which will be made clear in Fig. 14.

The important quantities for characterizing the noise source spectrum, and hence the cyclic correlation functions, are the boundary-layer thickness δ and the friction coefficient C_f, which appear in the boundary layer spectrum model in Eq. (34). The effect of these parameters on the cyclic correlations functions is presented below.

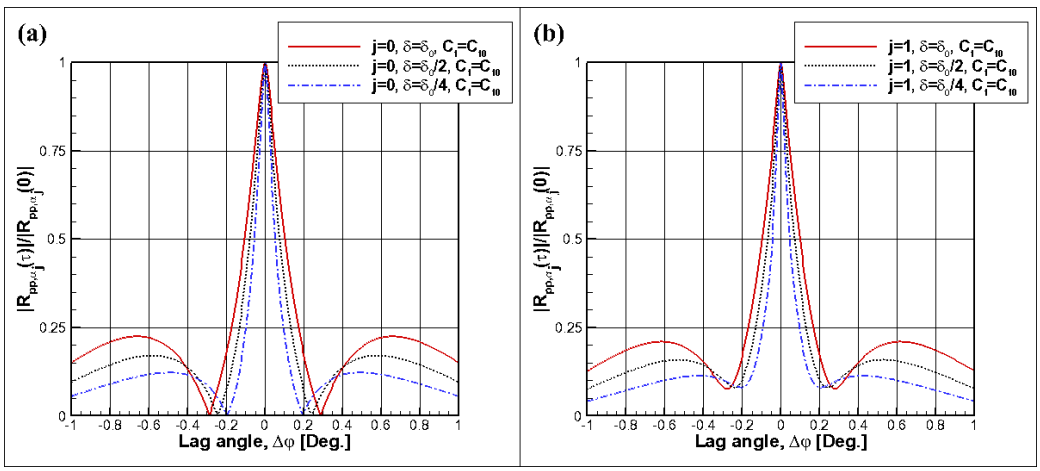

Fig. 14 Variation of cyclic autocorrelation functions versus the boundary layer displacement δ and the friction coefficient C_f.

Figure 14 shows the sensitivity of the predicted cyclic autocorrelation functions to the boundary-layer thickness δ. As δ is reduced the cyclic auto correlation functions become narrower around the zero-lag angle and thus τ_{half} $(= \delta/U_X)$ decreases. Note that very little effect on the CAC was observed due to changes in frictional coefficient. The reason for this can be explained by the much higher sensitivity of the radiated noise to δ compared with C_f, which affects the boundary layer pressure only at high frequencies.

The CAC functions therefore relate to the source characteristics and not the propagation. In the present case, δ/U_X controls the bandwidth of the CAC functions, as shown in Figure 14.

The value of cyclic auto correlation at $\tau = 0$ corresponds to the mean square pressure (variance) in each cyclic order. Using the relations of Eqs. (9), (10) and (15);

$$\overline{p_{\alpha_j}^2} = \mathcal{R}_{pp,\alpha_j}(0) \qquad (36)$$

Figure 15 compares the predicted and measured cyclic-spectral distribution of the acoustic pressure instantaneous variance computed using Eq. (36) normalized by their respective values at $j = 0$. Good overall agreement is obtained although there is a relatively larger discrepancy in the dominant first cyclic order.

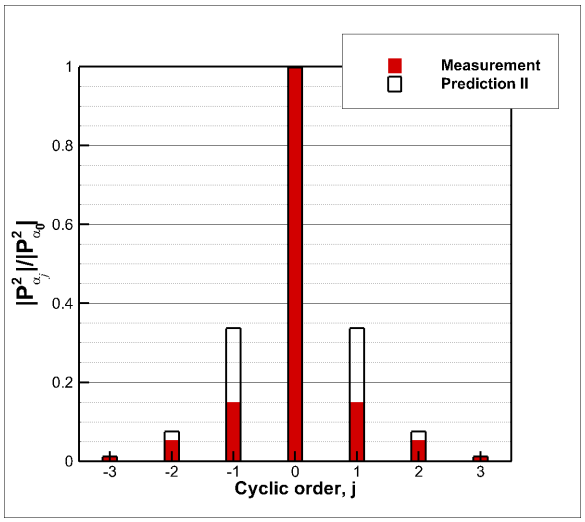

Fig. 15 Comparison of normalized cyclic spectral distributions between the prediction and measurement

Figure 16 presents the time-variation of instantaneous mean square pressure reconstructed from $\mathcal{R}_{pp}(t,\tau=0) = \sum_{\alpha_j} \mathcal{R}_{pp,\alpha_j}(\tau=0)e^{i2\pi\alpha_j t}$ using the cyclic spectral components $\mathcal{R}_{pp,\alpha_j}$ up to $j=3$. Note that the phase of the predicted time variation of signals is adjusted to give the best match to the time of maximum mean square pressure. Reasonable qualitative agreement between the measured and predicted time variations are obtained with the predicted swishing amplitude found to be about 30% less than the measured variation.

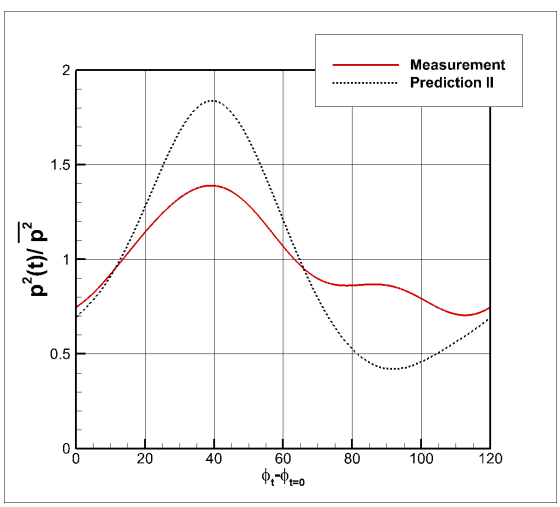

Fig. 16 Reconstructed time-variation of mean square pressure

Predictions of the time-frequency variation of the radiated acoustic pressure spectrum was calculated from Eq. (26) and plotted in Fig. 17. At frequencies below about 1kHz, small

variations in radiated noise can be seen. However, since the levels in this frequency range are significantly higher than at higher frequencies, this low frequency variation determines the overall mean square pressure variation. At higher frequencies, two distinct peaks in the angular noise variation can be observed with a minimum location corresponding to a blade position at around $\phi = 60°$ evaluated with respect to observer time. Figure 21 shows that this angle

corresponds to a blade angle of 180 degs evaluated with respect to source time. Note that these angles will vary for different rotation speeds and observed position. A fuller analysis of the mechanism for these peaks is provided below. The two peaks are predicted to become narrower as the frequency is increased along with an increase in the number of smaller oscillations away from the main peaks.

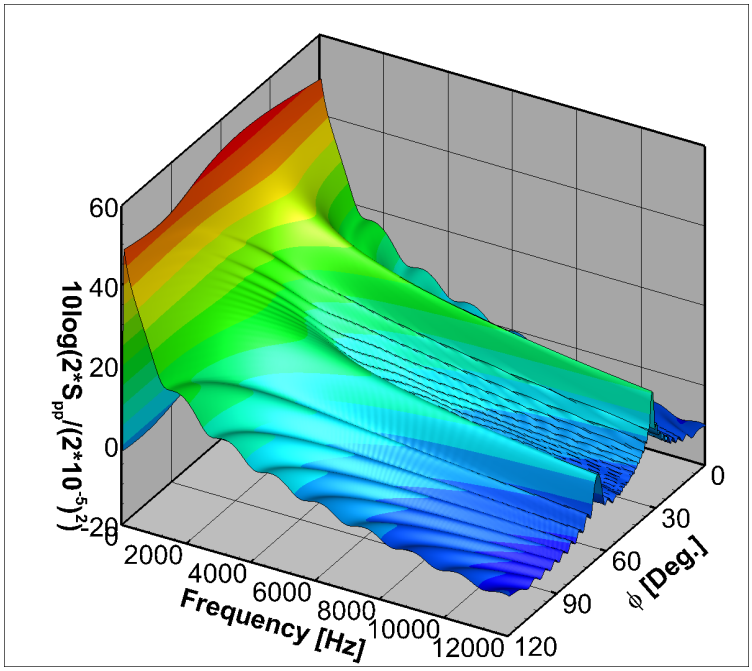

Fig. 17 Time-variation of acoustical pressure sound power spectral density levels

The predicted time-frequency spectrum is now compared directly to the measured Wigner-Ville spectrum in Fig. 18. Although the predicted levels generally overestimate the measured levels, similar time-frequency swishing behaviors can be observed. In both cases two distinct angular peaks are observed above about 2000 Hz with the first peak being slighly stronger than the second.

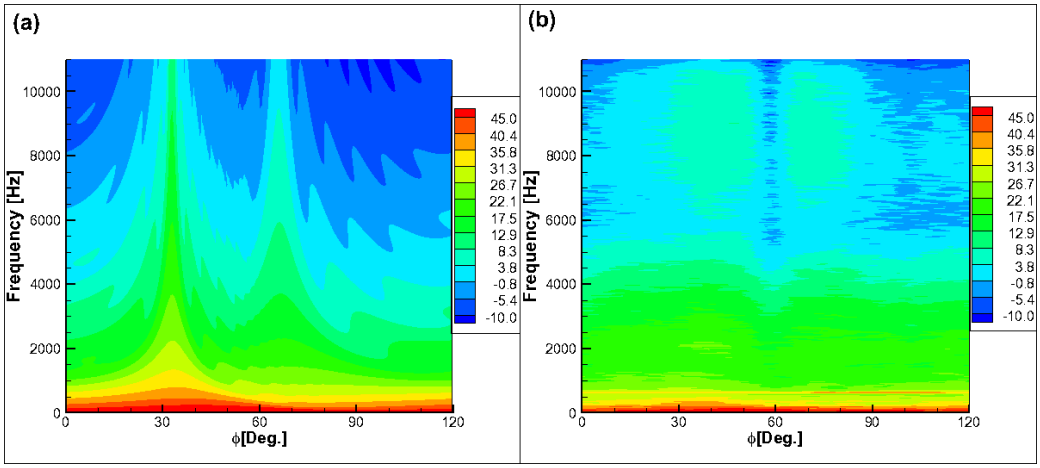

Fig. 18 Comparison of (a) predicted and (b) measured time-frequency sound power spectral density levels

A clearer comparison between the measured and predicted time-variation of mean square pressure is presented in Fig. 19 showing the same data in Fig 18 integrated over the mid and high-frequency bandwidths identified in Fig 2.

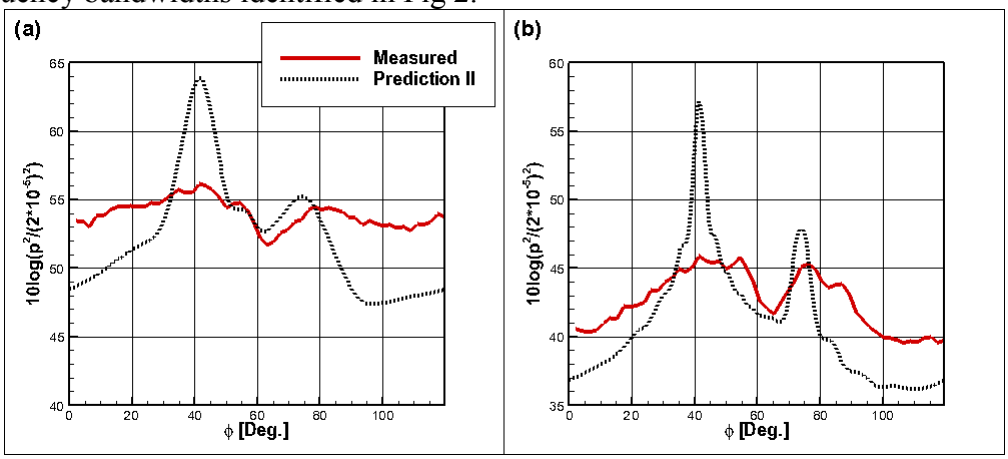

Fig. 19 Time-variation of mean squre pressure predicted and measured for the frequency bands (a) between 1750-5500 Hz and (b) above 5500 Hz

The predicted peaks are about 10dB higher than the measured levels. However, the general behaviour with blade angle is well captured by the model. The theory developed in Section 5 is now further analyzed to determine the main factors which influence the time varying high-frequency spectral characteristics referred to as 'swishing'. Eq. (26) may be separated into the following terms:

$$S_{pp}(r_0,\psi_0,\theta,\omega,\phi_t) = D^+(r_0,\psi_0,\theta,\phi_t)L(r_0,\psi_0,\theta,\omega,\phi_t)\omega^2 S_{qq}(r_0,\psi_0,\theta,\omega,\phi_t) \quad (37)$$

where

$$D^+(r_0,\psi_0,\theta,\phi_t) = \frac{1}{2\pi}\left(\frac{\omega_{\phi_{t'}}}{\omega}\right)^3\left(\frac{cr_0}{2c_0\sigma^2}\right)^2 \Delta r D_{\phi_{t'}}(\theta,a,\psi_0) \quad (38)$$

and

$$L(r_0, \psi_0, \theta, \omega, \phi_t) = \left|\mathcal{L}\left(k_{r,\phi_{t'}}, K_{x,\phi_{t'}}, \kappa_{\phi_{t'}}\right)\right|^2. \qquad (39)$$

The last term $\omega^2 S_{qq}$ in Eq. (37), associated with the boundary layer surface pressure spectrum, is much less sensitive to the blade position. The remaining terms in Eqs. (38) and (39) are plotted versus frequency and blade angle in Fig. 20 where it may be observed that the high-frequency swishing characteristics observed in Figs. 17 to 19 are mainly due to the behavior of the blade unsteady loading function, $|\mathcal{L}|^2$ that exhibit nearly all of the same behavior with blade angle as the noise radiation plotted in Fig. 17. The low-frequency swishing behavior observed in Fig. 17 is, however, dominated by the function D^+ in Eq. (38), which also determines the overall swishing character of wind turbine noise due to its dominance of the spectrum.

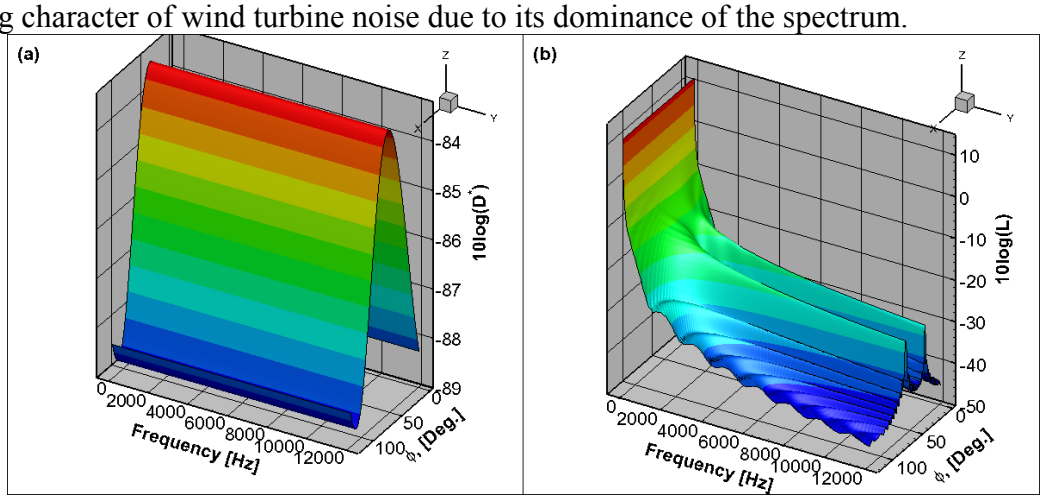

Fig. 20 Decomposition analysis: (a) D^+, and (b) L

At sufficiently high frequency the loading function of Eq. (30) can be approximated by,

$$\mathcal{L}(k_r, k_x, \kappa) \cong \frac{1}{\Theta_2}\sqrt{\frac{\Theta_1}{\Theta_1 - \Theta_2}} \qquad (40)$$

Figure 21 compares the approximate and exact behaviors of L defined in Eq. (39), computed using the exact and approximate formulations for the loading function at three specific frequencies, respectively. Note that the results in Fig. 21 are obtained using the contribution of single blade at the source time instead of summing all of the contributions from three blades at the observer time. This result makes clear that the radiation peaks observed in Figs. 18 and 19 occur at angles for which $\Theta_1 = \Theta_2$. It is seen that the locations of peak amplitude appear

independent of frequency with a minimum angular location at around $\phi' = 180°$ defined with respect to source time.

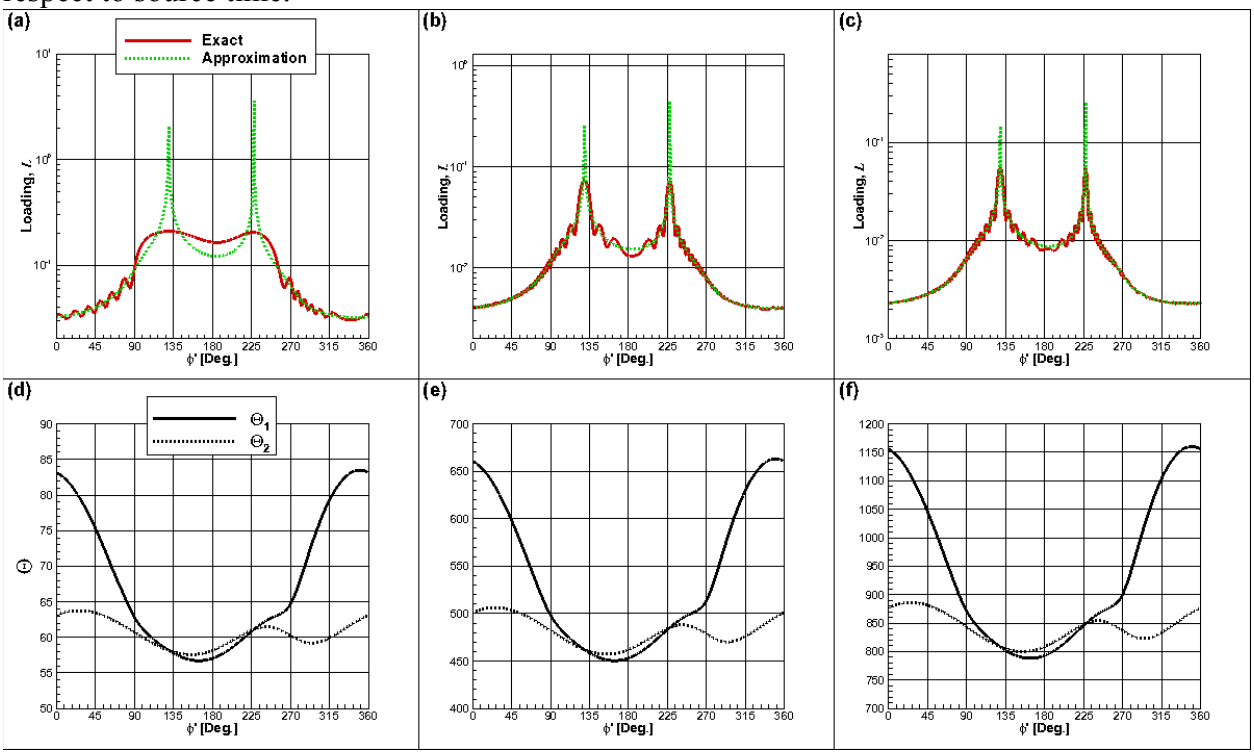

Fig. 21 Variation of a loading function and its input arguments during one rotation at a constant frequency for a receiver at $(x, y, z) = (15, 0, -62)$ m: (a) & (d) 500 Hz, (b) & (e) 4000 Hz, and (c) & (f) 7000 Hz

Combining Eq. (31) with Eqs. (25) and (20) and substituting into the condition, $\Theta_1 = \Theta_2$, the following expression is obtained for the time (or blade angle ϕ') at which peak radiation occurs,

$$\sqrt{1 - \beta_X^2 \left[\frac{r - \bar{r}}{\sigma}\right]^2} + M_x = D_p \left(M_X - \frac{X}{\sigma}\right) \qquad (41)$$

Two important observations can be made from Eq. (41). First, the blade angle for which $\Theta_1 = \Theta_2$ is a function of the receiver position and the flow and blade speeds, but independent of frequency (as already implied in the discussion about the result in Fig. 21). Second, if the Doppler effect is neglected. i.e., $D_p = 1$, there is no real solution to Eq. (41) for the blade angle.

In other words, the observed double-peak phenomenon does not occur in the time-frequency

noise spectrum due to a stationary blade in a steady mean flow.

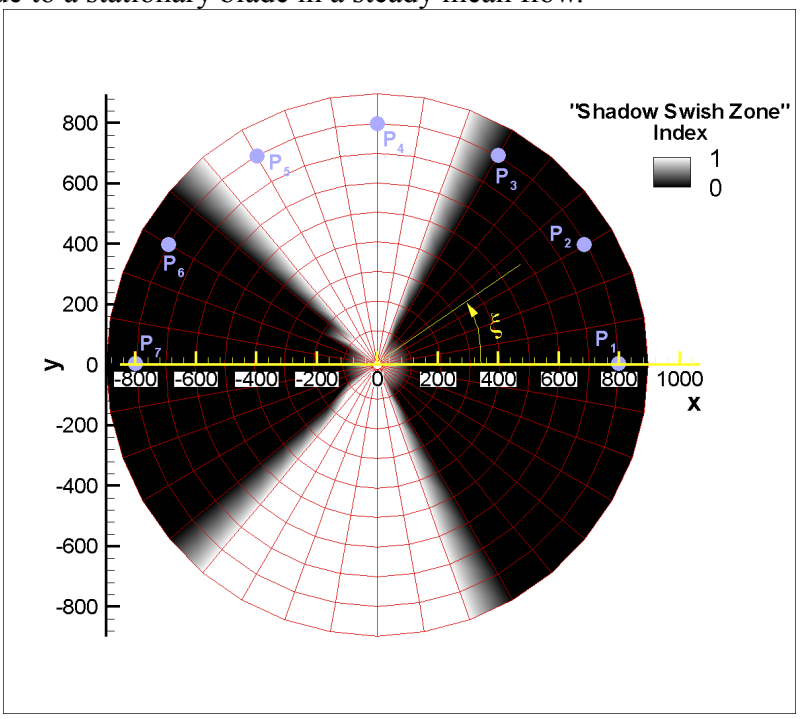

Fig. 22 Predicted "shadow swish zone" on the ground level (z= $-62\ \mathrm{m}$): computation is performed on the mesh of $(x, y) = \left((98 \times n + 15) \times cos(10° \times m), (98 \times n + 15) \times sin(10° \times m)\right)\ \mathrm{m}$, where *n=0:9* and *m=0:36*.

Equation (41) defines a 'shadow swish zone' in which the double-peak behavior observed previously cannot exist, where the plane of rotation is along the $x = 0$ plane and the axial flow direction is in the positive x - direction. Figure 22 presents the predicted noise map evaluated on the ground ($z = -67\ \mathrm{m}$) in the vicinity of the wind turbine. The white area denotes the regions where the radiation contains two peaks whereas black area denotes the shadow swish zone where two-peak behavior cannot exist. Except for the locations very near the wind turbine, the shadow swish zone is spread over the range of upstream angles, $140° < \xi < 220°$, and downstream angles, $-70° < \xi < 70°$ of the wind turbine. Here, $\xi = \mathrm{atan}(y/x)$ is defined in Fig. 22. However, for the receiver located around near the plane of rotation, $x = 0$ on the ground, there are always two blade positions for which $\Theta_1 = \Theta_2$, irrespective of the distance between the receiver and the center of a rotor.

To investigate the physical condition that give rise to these peaks, Eqs. (21) - (22) are substituted into Eq. (41) and rearranged to give,

$$M_{\phi R_0} = \frac{\sqrt{1-\beta_X^2\left[\frac{r-\bar{r}}{\sigma}\right]^2} + X/\sigma}{\sqrt{1-\beta_X^2\left[\frac{r-\bar{r}}{\sigma}\right]^2} + M_x} \qquad (42)$$

which suggests that the peaks occur when the component of blade rotation Mach number in the direction of the observer, $M_{\phi R_0}$, is equal to the term on the right-hand side of Eq. (42).

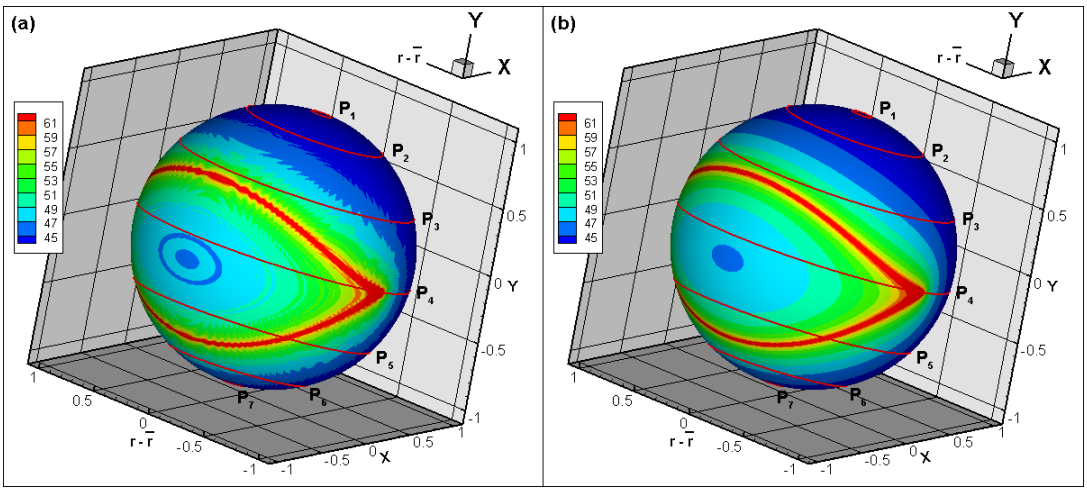

Fig. 23 Directivity spheres computed using the exact (a) and approximate (b) loading functions with the projected trajectories of the observer locations denoted by 'P' shown in Fig. 22: the contour values equal to $10 \times \log(L \times \omega_\phi^2)$.

In order to assess the influence of the loading function L in Eq. (39) in combination of the Dopper factor on the two-peak phenomenon and thus high-frequency swish character, it is useful to know the position of an observer in a blade-fixed coordinate together with the directivity due to the L function. For this purpose, the trajectories of the observer locations on the directivity sphere, during one revolution of the blade, are projected on the high-frequency directivities computed using the exact and asymptotic form of loading functions, respectively in Fig. 23. The computed directivities are normalized by ω_ϕ^2, and the exact directivity of L is computed at the frequency of 10,000 Hz. In fact, the normalized exact function $L \times \omega_\phi^2$ is a very weak function of a frequency in the high frequency range and the normalized approximate loading function of Eq. (40) is independent of frequency. It can be seen that the two predicted directivities are in close agreement and that each observer location denoted by 'P' in Fig. 22 follows a circle at more or

less constant 'latitude' $\beta(=\sin^{-1}\left(\frac{Y}{R_0}\right))$ where β depends on the observer's angle ξ. The three upper circles in Fig. 23 represent the trajectories of observer locations P_1 to P_3 in Fig. 22 in a blade-fixed coordinate, while the three lower circles correspond to the downwind locations P_5 to P_7. Figure 23 illustrates that the high-frequency swishing character depends on the variation of the directivity levels along each circle. Thus, the high-frequency wind turbine noise perceived by an observer on the ground on a circle around the turbine is due to the directivity characteristics of the loading function in combination with the Doppler effect. The observed two-peak phenomenon occurs when the observer's circle intersects the peak radiation of the loading functions denoted by the red contours in Fig. 23. The observer position such as P_1, P_2, P_3, P_6 and P_7 whose corresponding circle doesn't meet the peak radiation contours belong to the shadow region, as shown in Fig. 22. The peak radiation contour lines are symmetric about the X-Y plane but asymmetric about the Y=0 plane because the blade velocity vector is asymmetric as $\overrightarrow{M_\phi} = \left(0, -M_\phi \sin(\alpha), M_\phi \cos(\alpha)\right)$ in the airfoil-bound coordinate.

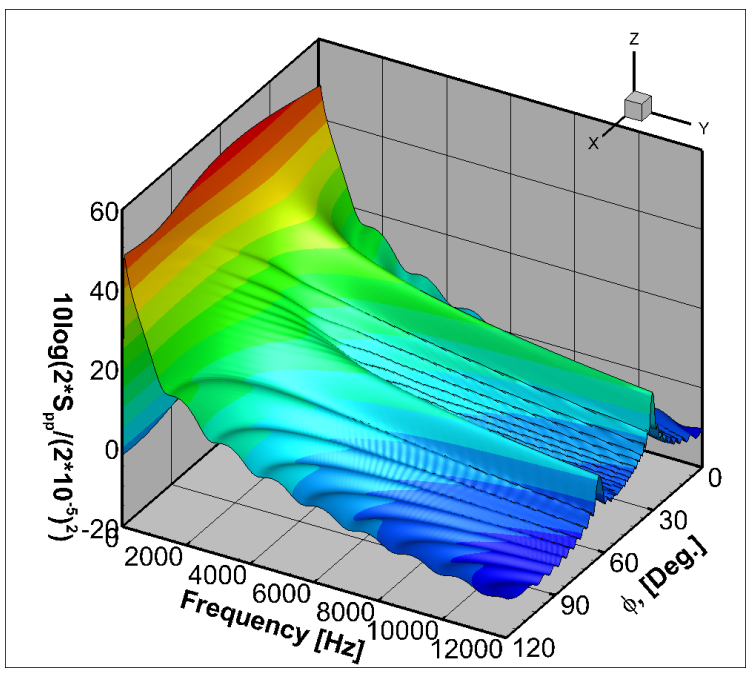

Fig. 24 Time-variation of acoustical pressure sound power spectral density levels for a receiver at $(x, y, z) = (30, 0, -62)$ m

Typical predictions of the time-frequency variation of acoustic pressure radiated to an obsever in shadow swish zone is plotted in Fig. 24. As predicted a single peak is observed in the high-frequency frequency range.

8. Conclusion

Cyclostationary analysis has been applied to the measured noise from a large modern upwind axial wind turbine. It has been shown that cyclostationary spectral analysis via its various time-

frequency representations has allowed the noise sources and their propagation character to be separately analyzed. The rotor self-noise model due to Amiet has been reformulated to allow direct comparison with the cyclostationary measurements and provides a prediction model for wind turbine noise. Prediction results using this model have been compared with the measured data. These comparisons reveal three important physical observations. First is that the length-scale involved in the cyclic auto correlation functions is related to those of boundary layer turbulence spectrum. The second is that bi-modal shapes in the time-frequency spectrum that are dominant in the high frequency range are due to the characteristics of the cyclic time variations in the unsteady blade loading function. The third is the overall swishing character is determined by the directivity functions. Finally, based on this analysis, a simple algebraic formula to approximate swishing index level (SWIL) has been derived to assess the swishing character of far field wind turbine noise. Predictions based on this formula show good agreement with exact calculations.

ACKNOWLEDGEMENT

This work was supported by the National Research Foundation of Korea Grant funded by the Korean Government (NRF-2011-013-D00018). This research was supported by Basic Science Research Program through the National Research Foundation of Korea (NRF) funded by the Ministry of Education (NRF-2013R1A1A2012672).

REFERENCES

[1] E. Pedersen and K. Persson Waye, Perception and annoyance due to wind turbine noise-A dose-response relationship, Journal of the Acoustical Society of America, 116 (2004) 3460-3470.

[2] F. van den Berg et al., WINDFARM perception: Visual and acoustic impact of wind turbine farms on residents – Final report, 2008

[3] P. Dunbabin, An investigation of blade swish from wind turbines, Proceeding of Internoise 96, 1996.

[4] G. P. van den Berg, The sounds of high winds, PhD thesis University of Groningen, The Netherlands, 2006.

[5] D. Bowdler, Amplitude modulation of wind turbine noise, Acoustics Bulletin of the Institute of Acoustics (UK), Vol. 33, No. 4, July/August 2008.

[6] V. V. Lenchine, Amplitude modulation in wind turbine noise, Proceedings of Acoustics 2009, 2009.

[7] Di Naploi, Wind turbine noise in a small and quiet community in Finland, Noise Control Engineering Journal, Vol. 59, Issue 1, pp. 30-37, 2011.

[8] S. Oerlemans, J. G. Schepers, Prediction of wind turbine noise and validation against experiment,

International Journal of Aeroacoustics, Vol. 8, No. 6, 2009.

[9] J. Antoni et al., Cyclostationary Modelling of Rotating Machine Vibration Signals, Mechanical Systems and Signal Processing, Vol. 18, No. 6, 2004, pp. 1285-1314.

[10] F. Bonnardot, Extraction of Second-Order Cyclostationary Sources: Application to Vibration Analysis, Mechanical System and Singal Processing, Vol. 19, No. 6, 2005, pp. 1230-1244.

[11] V. Jurdic, P. Joseph, J. Antoni, Investigation of Rotor Wave Turbulence Through Cyclostationary Spectral Analysis, AIAA Journal, Vol. 47, No. 9, 2009, pp. 2022-2030.

[12] J. C. Hardin and A. G. Miamee, Correlation Autoregressive Processes with Application to Helicopter Noise, Journal of Sound and Vibration, Vol. 142, 1990, p. 2.

[13] W. A. Gardner, A. Napolitano, A. Paura, Cyclostationarity: Half a Century of Research, Signal Processing, Vol. 86, No. 4, 2006, pp. 639-697.

[14] R. K. Amiet, Noise produced by turbulent flow into a Propeller or Helicopter Rotor, AIAA Journal, Vol. 15, No. 3, 1977, pp. 307-308.

[15] V. P. Blandeau, P. F. Joseph, Validity of Amiet's Model for Propeller Trailing-Edge Noise, AIAA Journal, Vol. 49, No. 5, 2011.

[16] J. E. Ffowcs Williams, D. L. Hawkings, Theory Relating to the Noise of Rotating Machinery, Journal of Sound and Vibration, Vol. 10, No. 1, 1969, pp. 12-21.

[17] G. Homicz, A. George, Broadband and Discrete Frequency Radiation from Subsonic Rotors, Journal of Sound and Vibration, Vol. 36, No. 2, 1974, pp. 151-177.

[18] C. Osborne, Unsteady Thin-Airfoil Theory for Subsonic Flow, AIAA Journal, Vol. 11, No. 2, 1973, pp. 205-209.

[19] Y. N. Kim and A. R. George, Trailing-Edge Noise from Hovering Rotors, AIAA Journal, Vol. 20, No. 9, 1982, pp. 1167-1174.

[20] R. K. Amiet, Noise produced by Turbulent Flow into a Propeller or Helicopter Rotor, AIAA Journal, Vol. 15, No. 3, 1977, pp. 307-308.

[21] S. Sinayoko, M. Kingan, A. Agarwal, Trailing edge noise for rotating blades: analysis and comparison of two classical approaches, AIAA-2012-2302, 2012.

[22] R. A. Boyles, W. A. Gardner, Cycloergodic Properties of Discrete-Parameter Nonstationary Stochastic Processes, IEEE Transactions on Information Theory, Vol. 29, 1983, pp. 105-114.

[23] S. Braun, The Extraction of Periodic Waveforms by Time Domain Averaging, Acustica, Vol. 32, No. 2, 1975, pp. 69-77.

[24] W. Martin, P. Flandrin, Wigner-Ville Spectral Analysis of Nonstationary Processes, IEEE Transactions on Acoustics, Speech, and Signal Processing, Vol. ASSP-33, No. 6, pp. 1461-1470, 1985.

[25] S.-S. Jung, W.-H. Cheung, C. Cheong, S.H. Shin, Experimental identification of acoustic emission on infrasound and low-frequency noise, Journal of the Korean Physical Society, Vol. 53, No. 4, 2008, pp. 1897-1905.

[26] G.-S. Lee, C. Cheong, S.-H. Shin, S.-S. Jung, A Case Study of Localization and Identification of Noise Sources From a Pitch and a Stall Regulated Wind Turbine, Applied Acoustics, Vol. 73(8), 2012, pp. 817-827.

[27] M. V. Lowson, The sound field for Singularities in Motion, Proceedings of the Royal Society of London, Series A, Mathematical and Physical Science, Vol. 286, No. 1407, 1965, pp. 559-572.

[28] R. K. Amiet, Noise due to Turbulent Flow Past a Trailing Edge, Journal of Sound and Vibration, Vol. 47, No. 3, 1976, pp. 387-393.

[29] R. K. Amiet, Effect of the Incident Surface Pressure Field on Noise due to Turbulent Flow Past a Trailing Edge, Journal of Sound and Vibration, Vol. 57, No. 2, 1978, pp. 305-306.

[30] M. Roger, S. Moreau, Back-Scattering Correction and Further Extensions of Amiet's Trailing-Edge Noise Model, Part 1: Theory, Journal of Sound and Vibration, Vol. 286, No. 3, 2005, pp. 477-506.

[31] T. F. Brooks, T. H. Hodgson, Trailing Edge Noise Prediction from Measured Surface Pressure, Journal of Sound and Vibration, Vol. 78, No. 1, 1981, pp. 69-117.

[32] M. Goody, Empirical Spectral Model of Surface Pressure Fluctuations, AIAA Journal, Vol. 42, No. 9, 2004, pp. 1788-1794.

[33] S. Oerlemans, P. Sijtsma, B. Mendes Lopez, Location and quantification of noise sources on a wind turbine, Journal of Sound and Vibration, Vol. 299, Issues 4-5, 2007, pp. 869-883.

[34] M. Drela, XFOIL: An analysis and design system for low Reynolds number airfoils, Low Reynolds number aerodynamics, T. J. Muller, Ed., University of Notre Dame, Paris, 1989.

[35] V. Blandeau, Aerodynamic broadband noise from contra-rotating open rotors, Ph. D. thesis, University of Southampton, 2011.

[36] Y. Rozenberg, G. Robert, S. Moreau, Wall pressure spectral model including the adverse pressure gradient effects: application to the prediction of trailing-edge noise, AIAA J., Vol. 50, No. 9, 2012, pp.

2168-2179

[37] G.-S. Lee, C. Cheong, Frequency-domain prediction of broadband trailing edge noise from a blunt flat plate, Journal of Sound and Vibration, Vol. 332, Issue 21, 2013, pp. 5322–5344.